Nanostructured Intermetallic Nickel Silicide (Pre)Catalyst for Anodic Oxygen Evolution Reaction and Selective Dehydrogenation of Primary Amines

Indranil Mondal, J. Niklas Hausmann, Gonela Vijaykumar, Stefan Mebs, Holger Dau,* Matthias Driess,* and Prashanth W. Menezes*

The development of novel earth-abundant metal-based catalysts to accelerate the sluggish oxygen evolution reaction (OER) is crucial for the process of large-scale production of green hydrogen. To solve this bottleneck, herein, a simple one-pot colloidal approach is reported to yield crystalline intermetallic nickel silicide (Ni_2Si), which results in a promising precatalyst for anodic OER. Subsequently, an anodic-coupled electrosynthesis for the selective oxidation of organic amines (as sacrificial proton donating agents) to value-added organocyanides is established to boost the cathodic reaction. A partial transformation of the Ni_2Si intermetallic precatalyst generates a porous nickel(oxy)hydroxide phase modified with oxidic silicon species as unequivocally demonstrated by a combination of quasi in situ Raman and X-ray absorption spectroscopy as well as ex situ methods. The activated form of the catalyst generates a geometric current density of 100 mA cm^{-2} at an overpotential (η_{100}) of 348 mV displaying long-term durability over a week and high efficiency in paired electrolysis.

1. Introduction

Water electrolysis is one of the promising approaches to convert renewable electricity to green chemical fuels and is a key pro-

cess toward a circular economy.[1] Water electrolysis consists of two electrochemical half-reactions: the hydrogen evolution reaction (HER) to produce hydrogen at the cathode and the OER to evolve oxygen at the anode, respectively. While the HER is a relatively straightforward two-electron transfer process, the main bottleneck is the sluggish four-electron OER that limits the overall efficiency of water electrolysis.[2,3] Currently, the common and matured industrialized electrolyzers to produce hydrogen rely on either acidic (proton-exchange membrane) or alkaline conditions. Out of which, alkaline electrolyzers are of particular importance as they use low-cost and earth-abundant materials to make the system fully sustainable and economically competitive.[4]

As stated above, in order to increase the efficiency of the electrolyzers, improved anodes with high intrinsic activity are required. Notably, for alkaline electrolyzers, Ni-based materials have been the typical choice as anode (OER) materials because of their cost-effectiveness, high elemental abundance, good resistance to corrosive solutions, and low toxicity.[5,6] In recent years, significant progress has been achieved in the design, synthesis, and development of a variety of highly efficient Ni-based electrocatalysts involving oxides/hydroxides, chalcogenides, pnictides, alloys, and even metal-organic frameworks for OER at the lab scale to minimize the energetic losses in alkaline electrolysis.[6–11] Besides, significant efforts have been made to modify Ni-based electrocatalysts through heterostructure formation, oxygen-defect generation, doping with heteroatoms, as well as phase and morphology engineering to attain technically viable efficiencies. However, further improvement beyond the current state of the art is required to enhance the overall OER performance.[9–14]

Most of the Ni-based catalysts transform under the electrochemical alkaline conditions into electronically similar layered oxyhydroxide (LOH) phase with $Ni^{III}O_xH_y$ structure.[15,16] Similar to other transition-metal electrocatalysts, the OER activity of Ni-based catalysts largely depends on the defects, surface area, morphology, crystal structure of the precatalyst (e.g., Ni—Ni distances), amount of edge/corner-sharing $[NiO_6]$ units, size of the crystallite domain, etc. of the transformed $Ni^{III}O_xH_y$ phases,

I. Mondal, J. N. Hausmann, G. Vijaykumar, M. Driess, P. W. Menezes
Department of Chemistry: Metalorganics and Inorganic Materials
Technische Universität Berlin
Straße des 17 Juni 135, Sekr. C2, 10623 Berlin, Germany
E-mail: matthias.driess@tu-berlin.de

S. Mebs, H. Dau
Fachbereich Physik
Freie Universität Berlin
Arnimallee 14, 14195 Berlin, Germany
E-mail: holger.dau@fu-berlin.de

P. W. Menezes
Materials Chemistry Group for Thin Film Catalysis – CatLab
Helmholtz-Zentrum Berlin für Materialien und Energie
Albert-Einstein-Str. 15, 12489 Berlin, Germany
E-mail: prashanth.menezes@mailbox.tu-berlin.de

The ORCID identification number(s) for the author(s) of this article can be found under https://doi.org/10.1002/aenm.202200269.

which differs with the mode of transformation and nature of the precatalyst.[17,18] Unfortunately, the transformed $Ni^{III}O_xH_y$ phases suffer from unfavorable Tafel slopes, thus demanding inflated overpotential to generate high current density.[19] Therefore, it is of utmost importance to search for novel, highly active, and robust Ni-based catalysts that can transform under electrocatalytic alkaline conditions to yield an active $Ni^{III}O_xH_y$ phase.

In this regard, intermetallic compounds are an interesting class of compounds for electrocatalytic OER as they possess ordered structures with intermediate bonding nature (between ionic and covalent), which are different than those of the constituent elements.[20,21] Our recent investigations on intermetallic compounds have shown that they transform partially or completely during harsh alkaline OER to electronically similar LOH structures.[17,22–25] Nevertheless, these LOH species are structurally and morphologically different and are responsible for varied electrolyte diffusion, electrochemical surface area, and surface versus bulk activity. Here, the leaching of ions is unavoidable and plays a major structure-determining role in the evolution of LOH species. Considering the natural abundance of Si, low electrical resistivity (10–24 $\mu\Omega$ cm), nature of chemical bonds between Ni and Si (e.g., weak Ni(d)-Si(p) interaction), and electrochemical Pourbaix diagram of Ni and Si, the Ni—Si intermetallic system could be a suitable and facile source to generate highly active LOH species (e.g., $Ni^{III}O_xH_y$) during OER.[26–28] However, like other intermetallics, the common solid-state synthesis of nickel silicides also involves an energy-intensive high-temperature process that often leads to high polydispersity, large aggregations, low surface area, phase impurities, passivating oxide layers on the metal silicide nanoparticle (NP), and undesired by-products which may affect the overall catalytic performances.[29,30] This motivated us to apply a unique colloidal approach to achieve the low-temperature formation of nickel silicide nanostructures with controlled solvation and nucleation, low polydispersity, and high phase purity.

Alternatively, pairing water splitting with organic transformation to value-added products (electrosynthesis) has been one of the thriving research topics in the last couple of years. In this context, choosing electrooxidative dehydrogenation of primary amines to cyanides is of special interest, mostly because i) sacrificial proton donating amines could boost up the HER at the cathode,[31] and ii) cyanides are valuable synthones for carboxylic acids, esters, aldehydes, imines, heterocycles, oximes, etc.[32] To date, the synthesis of cyanides mostly involves the nucleophilic substitution of halide with highly toxic cyanide ions,[33] or ammoxidation process, which is inherently limited by the poor functional group tolerance due to harsh reaction conditions (300–350 °C).[34] Direct electrooxidation of amines in aqueous alkaline media avoids these difficulties and provides an opportunity for industrial-scale cyanides production sustainably.[35]

In view of the above, the current work addresses and answers the following questions: i) Can one synthesize homogeneously distributed well-defined intermetallic nickel silicide (Ni—Si) nanostructure avoiding high-temperature solid-state methods? ii) Is this Ni—Si active and durable for OER? iii) Can a phase transformation be uncovered by in situ spectroscopy (Raman, X-ray absorption spectroscopy (XAS)) and how does Si behave under the OER condition? iv) How can leaching ions (e.g., Si) control over the redox behavior of active structure as compared to that generated from a (pre)catalyst with no leaching ion? v) Is the in situ formed active phase also suitable for multielectron oxidations of organic compounds such as dehydrogenation?
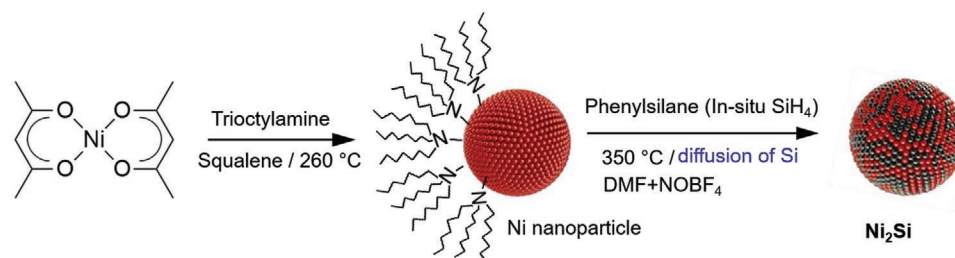
Herein, we report the synthesis of ordered Ni_2Si NPs using a one-pot colloidal approach and utilized it as an OER electro(pre)catalyst. Under alkaline conditions, the intermetallic Ni_2Si transformed into $Ni^{III}O_xH_y$ phase as an active phase by concomitant corrosion of Si to silicate. To uncover the correlation between Si leaching during electrochemical transformation and its catalytic activity, we carried out quasi in situ XAS together with Raman spectroscopy on Ni_2Si NPs treated under OER condition and compared it with metallic Ni NPs having similar morphology and electronic properties. The activated form of the catalyst not only generated a low overpotential of 348 mV at 100 mA cm^{-2} (η_{100}) in OER but was also effective for selective dehydrogenation of primary amines to nitriles with very high efficiency.
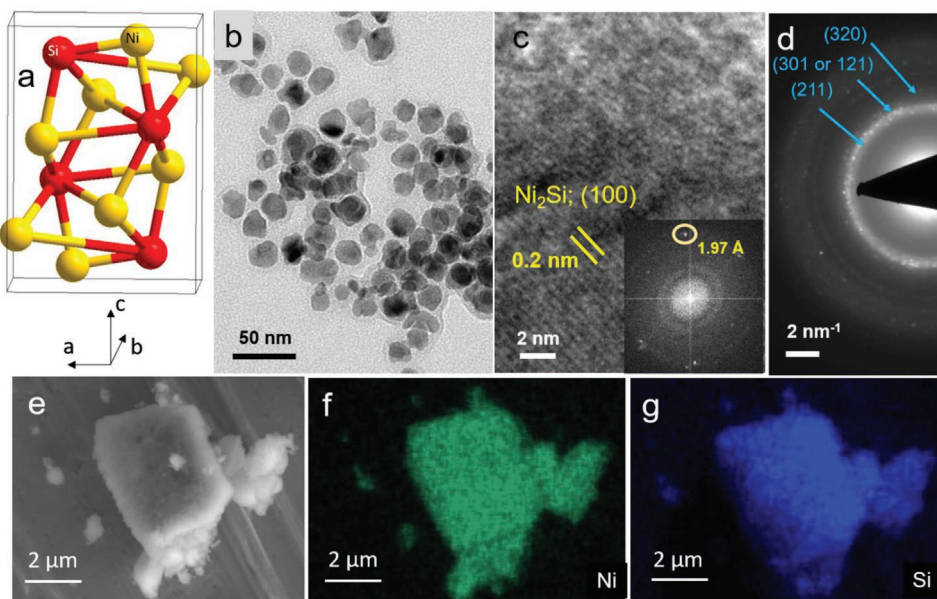
2. Results and Discussion

2.1. Synthesis and Structural Features

Ni_2Si NPs were synthesized using a low-temperature one-pot two-step colloidal approach (**Scheme 1**). In the first step, thermal reduction of nickel(II) bis(acetylacetonate) in the presence of n-trioctylamine and n-trioctylphosphine led to the formation of Ni^0 NPs. In the subsequent step, the NPs were subjected to silicidation using phenylsilane to form Ni_2Si (see Supporting Information for a detailed synthetic procedure).

The formation of Ni_2Si NPs can be attributed to its high interdiffusion coefficient at lower silicidation temperatures.[36] This is in compliance with the thermodynamic phase stability of the

Scheme 1. Schematic illustration of the synthesis of Ni_2Si NP using a colloidal approach.

**ADVANCED
SCIENCE NEWS**

www.advancedsciencenews.com

**ADVANCED
ENERGY
MATERIALS**

www.advenergymat.de

Figure 1. Structural characterization of intermetallic Ni_2Si. a) Crystal structure of Ni_2Si depicting four Si (red spheres) and eight Ni (yellow spheres) atoms in the unit cell (gray lines). b) TEM, c) HRTEM, and d) SAED pattern of Ni_2Si NP. The NPs are distorted spherically shaped with an average size of 20 nm. The HRTEM reveals the exposed (100) facet of a single NP. Nonetheless, Ni_2Si showed multifaceted morphology with polycrystalline in nature as supported by typical ring pattern SAED. (211), (121), and (320) were clearly identified in the SAED pattern. e) Selected area SEM image of Ni_2Si and corresponding mapping for f) Ni and g) Si shows the homogeneous distribution of the constituent's elements.

Ni—Si system (Figure S1, Supporting Information). The powder X-ray diffraction (PXRD) pattern revealed the presence of a pure crystalline Ni_2Si phase (Figure S2, Supporting Information) that crystallizes in the orthorhombic space-group *Pnma* (62) and thus belongs to *oP*12 structures (**Figure 1**a, Figure S3; Table S1, Supporting Information). The unit cell consists of 12 atoms (4 Si and 8 Ni atoms) with eight different sets of direct Ni—Si bonds with lengths ranging from 2.0823–3.9809 Å. The transmission electron microscopy (TEM) images of Ni_2Si show distorted spherical NPs with an average diameter of 20 nm. Lattice fringes resolved in high-resolution TEM (HR-TEM) measurements as well as the selected area diffraction pattern (SAED) confirm the presence of the pure Ni_2Si phase (Figure 1b–d). Scanning electron microscopy (SEM) and energy-dispersive X-ray (EDX) mapping images reveal aggregated Ni_2Si NPs with homogenously distributed Ni and Si (Figure 1e–g, Figures S4 and S5, Supporting Information). Furthermore, EDX quantification and inductively coupled plasma atomic emission spectroscopy (ICP-AES) confirm the Ni_2Si stoichiometry (Table S2, Figures S6 and S7, Supporting Information). Additionally, the chemical and electronic structure of Ni_2Si was evaluated by Raman and X-ray photoelectron spectroscopy (XPS), while the surface area was determined by Brunauer–Emmett–Teller (BET) method. To obtain a reference compound for the electrocatalytic measurements, the Ni NPs were isolated after the first step of the Ni_2Si synthesis and comprehensively characterized (Figures S8–S15, Supporting Information).

2.2. Electrochemical Performance

The as-prepared Ni_2Si precatalyst was deposited on nickel foam (NF) and fluorine-doped tin oxide (FTO) using electrophoretic deposition (EPD), which is a binder-free deposition technique. This procedure preserved the chemical structure of the Ni_2Si and the oxidation state of the constituent elements and led to the formation of homogenous films (Figures S16–S23, Supporting Information). The EPD time was correlated with the mass loading and film thickness of the catalyst on FTO substrate, which was optimized based on the linear sweep voltammetry (LSV) current (Figure S24, Supporting Information). The mass loading for FTO and NF was 0.4 ± 0.1 and 0.8 ± 0.1 mg, respectively. The measurements were carried out under iron-free 1 M KOH solution to avoid Fe inclusion from the electrolyte.[37] Ni_2Si did not alter its parent structure in the alkaline medium without applying a potential (Figure S25, Supporting Information). Before evaluating the electrochemical activities, CV cycles were recorded until current responses of the N^{II}/Ni^{III} redox potential (1.2–1.5 V_{RHE}) remain unchanged (Figure S26, Supporting Information). The difference between the 1st and consecutive cycles indicates the transformation of Ni_2Si precatalyst.[38,39] To compare the electrocatalytic activity, the metallic Ni NPs isolated before silicidation and NiOOH NPs, synthesized by reducing the $Ni(OH)_2$ in aqueous persulfate solution, were measured under identical condition (see Supporting Information, experimental section, and Figures S27–S29, Supporting Information). As displayed in **Figure 2**a, compared to Ni and NiOOH, the CV curves revealed substantially lower overpotentials (η) for Ni_2Si/NF, with η_{10} and η_{100} of 247 ± 3 and 348 ± 6 mV, respectively. Nevertheless, the steady-state Tafel slopes of all three compounds are comparable (Figure 2b), implying a similar nature of active sites for the Ni-based catalysts, which follow the same OER rate-determining step.[40,41] The long-term stability of the Ni_2Si/NF catalyst was measured by chronopotentiometry (CP) at 100 mA cm^{-2}, which exhibited almost steady η value of around 350 mV for 200 h (Figure 2c). In contrast, Ni/NF and NiOOH/NF showed
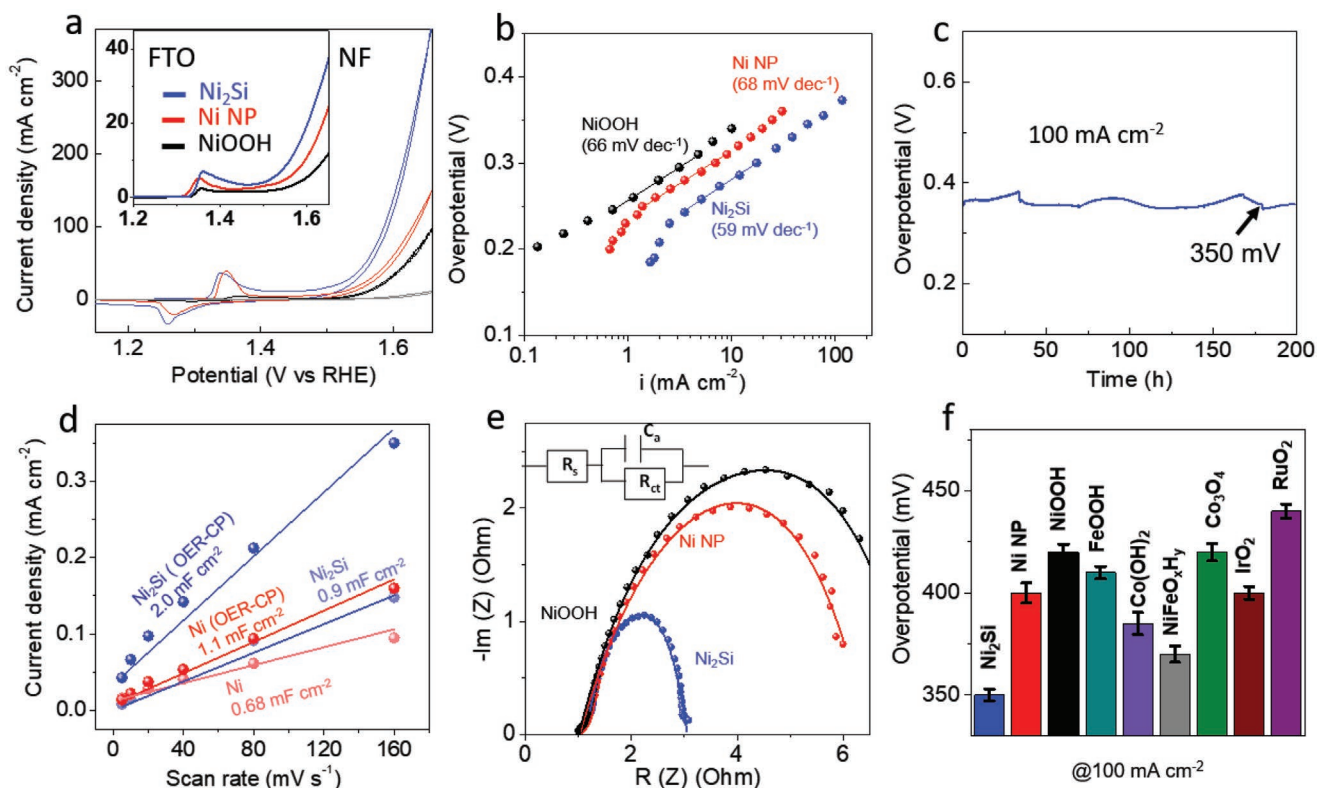
Figure 2. Electrocatalytic OER activities of Ni_2Si and nickel-based reference catalysts on NF electrodes in 1 M aqueous KOH electrolyte. a) The CV curve of Ni_2Si and other Ni-based catalysts on NF electrode at 1 mV s^{-1}. The measured η_{100} values are 348, 400, and 430 mV for Ni_2Si, Ni NP, and NiOOH respectively. The inset image shows the activity of the same catalysts on FTO under identical conditions yielding η_{10} values of 320, 361, and 412 mV for Ni_2Si, Ni NP, and NiOOH, respectively. b) Tafel slope of catalyst/NF electrode obtained from steady-state measurements applying a constant potential for 300 s with a step size of 15 mV. c) CP experiment of Ni_2Si/NF conducted at 100 mA cm^{-2}. d) The C_{dl} values extracted from the plot of (anodic current-cathodic current)/2 with respect to scan rate recorded before and after OER CP for Ni_2Si and Ni on NF. C_{dl} values are equal to the slope of the curves. e) EIS spectra of different catalysts measured at 1.55 V_{RHE}. The spectra were fitted using a Randles circuit with a constant phase element (inset). The fitted parameters were tabulated in Supporting Information (Tables S3 and S4, Supporting Information). f) Bar diagram (with error bars) displaying OER overpotentials at 100 mA. cm^{-2} of various as-prepared catalysts.

a deactivation during a 24 h CP measurement (Figure S30, Supporting Information). Furthermore, the long-term stability at a higher current density of 400 mA cm^{-2} was also measured for two days with no deterioration in OER activity its suitability for practical electrolysis (Figure S31, Supporting Information). To correlate the catalytic activity and the electrochemically active surface area (ECSA), the double layer capacitance (C_{dl}) values of the Ni_2Si, Ni, and NiOOH were measured after 24 h of OER CP at 100 mA cm^{-2}. The C_{dl} of a specific catalyst is qualitatively proportional to the ECSA,[42] and can be obtained from CVs with different scan rates measured in a non-Faradaic region. The extracted C_{dl} value of Ni_2Si is the highest among the Ni-based reference catalysts (Figures S32 and S33, Supporting Information). Interestingly, the C_{dl} values of Ni_2Si/NF and Ni/NF were almost the same before the CP measurement; however, the C_{dl} of Ni_2Si/NF increased significantly through the OER, making it more than two times larger than the one of Ni/NF after catalysis. This implies a larger surface transformation of Ni_2Si precatalyst (Figure 2d and Figures S34 and S35, Supporting Information). Moreover, the BET surface area normalized current density values of Ni_2Si/NF and Ni/NF did not alter the activity trends. However, the normalization with C_{dl} values resulted in

closer activity of Ni_2Si and Ni NP (Figure S36, Supporting Information). This indicates that the activity enhancement is majorly caused by more electrochemically active sites formed during surface transformation. The activity trends were further confirmed by the semicircle diameter of the Nyquist plots, recorded with electrochemical impedance spectroscopy (EIS) at 1.55 V. (Figure 2e and Figure S37, Supporting Information; The Nyquist plots were fitted with the simple equivalent Randles circuit model, yields both R_s and R_{ct}. Fitting parameters are tabulated in Tables S3 and S4, Supporting Information. To compare the activity with other reference anode catalysts, we synthesized a series of precious and non-noble-based catalysts and deposited them on NF using a similar method with approximately the same mass loading (0.8 ± 0.1 mg) (Figure 2f, Figures S38–S40, Supporting Information). Impressively, the Ni_2Si/NF electrode has the smallest η_{100} even in comparison to the well-known active layered $NiFeO_xH_y$ catalyst under identical OER conditions (Figure 2f). Furthermore, an OER Faradaic efficiency (FE) of 98 ± 3% was obtained for Ni_2Si/NF, which was determined by measuring the evolved O_2 gas (Figure S41, Supporting Information).

To rule out the contributions from the NF substrate, the electrochemical experiments were additionally performed on FTO.

The LSV current density, after OER C_{dl}, R_{ct} values follow the same trend as for NF (Figure 2a, Figures S42–S45, Supporting Information). The estimated steady-state Tafel slope values are also close (Figure S46, Supporting Information). Additionally, Ni_2Si/FTO electrode displayed excellent stability as continued to maintain an approximately steady potential of 1.55 V_{RHE} at 10 mA cm^{-2} over 4 days (Figure S47, Supporting Information). It is worth mentioning here that, as an alternative Ni_2Si synthesis method, one can isolate the Ni NPs to use them in a consecutive reaction for silicidation after purification using the conventional solvent-nonsolvent approach. We realized that with this method, the as-prepared Ni_2Si crystallite undergoes agglomeration to form larger particles, and subsequently, the current value was much lower (Figure S48, Supporting Information).

2.3. Post OER Ex Situ Characterization

To monitor the structural transformation and gather insights into the active form of the catalyst, we conducted OER-CP at 10 mA cm^{-2} for 24 h with Ni_2Si/FTO and subsequently characterized them. The SEM images after OER display a deep surface transformation of the precatalyst and the EDX spectrum shows a less intense peak for Si and a peak for O, suggesting the formation of an oxo-based structure (Figures S49–S51, Supporting Information). The resulting Ni:Si ratio is calculated to be 1:0.22 (ICP yield 1:0.26), confirming almost ≈50% loss of Si from the Ni_2Si precatalyst structure. Most notably, our results on the Ni_2Si electrodes under prolonged stability and at high current density under harsh OER operation conditions also confirmed that only a maximum of 50% of Si leaching is feasible from the structure (Figure S52, Supporting Information). After OER, the PXRD pattern showed weaker reflections of the Ni_2Si phase and no additional new peaks showing that some crystalline Ni_2Si remains and most likely a new oxidic amorphous phase has formed. (Figure S53, Supporting Information).[16,43] To obtain more information on the surface transformation, morphology, and structure, we scratched off Ni_2Si particles from FTO and recorded TEM. The TEM and HR-TEM images clearly exhibited typical core-shell features with a dense crystalline phase (≈ 10 nm) buried under an amorphous layer (**Figure 3** and Figure S54, Supporting Information). The corresponding scanning TEM (STEM) elemental mapping (Figure 3) revealed that the amorphous component is majorly composed of Ni-oxo species. The SAED profile extracted from the selected area TEM image displayed several diffuse rings (Figure S54, Supporting Information) and the estimated radius for the diffused rings confirms the presence of γ-NiOOH phase. The TEM EDX quantification confirmed the loss of Si (Figure S55, Supporting Information). In order to uncover the valence of Ni and Si in the post-reaction sample, a core-level XPS was recorded and compared with that of Ni treated under the same OER conditions (**Figure 4**a, Figure S56, Supporting Information). In the post-OER Ni_2Si, the deconvoluted Ni $2p_{3/2}$ profile correlates with Ni^{III} species.[44,45] The binding energy values obtained here for Ni^{III} are identical to γ-NiOOH phases reported in the literature.[46,47] On the other hand, metal-like Si states originating from Ni—Si bonds were not visible after OER, instead,

higher valent Si species (Si^{II}, Si^{IV}) were present (Figure S56, Supporting Information). Additionally, the O 1s spectra before and after OER confirms the presence of silicon-oxo (hydroxide or suboxide), nickel oxide, and nickel (oxy)hydroxide species. FT-IR spectroscopy after OER uncovered intense hydration of the catalyst film (Figure S57, Supporting Information). Pristine Ni_2Si has an IR band in the fingerprint region (around 580 cm^{-1}) which can be assigned to stretching vibrations of Ni—Si.[48] After OER, this band disappeared and a broad band was visible at around 650 cm^{-1}, which can be ascribed to Ni^{III}-O stretching vibrations of γ-NiOOH.[44,46,49] Additionally, the band centered at 1382 cm^{-1} can be attributed to carbon-oxygen stretching vibrations of CO_3^{2-}, which originates from dissolved CO_2 in KOH solution.[50] It has been previously shown that such CO_3^{2-} is intercalated into the γ-NiOOH layers which can be beneficial for the OER.[44,50]

2.4. Quasi In Situ Characterization

To correlate the structural transformation of Ni_2Si with the catalytic activity, we carried out in situ Raman and X-ray absorption on the freeze-quenched (−196 °C) samples. As prepared Ni_2Si exhibits no Raman active transitions above noise level within the measured spectral width (200–1000 cm^{-1}) (Figure 4b). The in situ Ni_2Si sample (treated under CP at 10 mA cm^{-2} for 24 h and freeze quenched at 1.58 V_{RHE}) contains two major bands at 481 and 561 cm^{-1} typical for the γ-NiOOH.[16,51] The peak centered at 481 cm^{-1} is associated with the depolarized E_g mode (bending vibration of the oxygen atoms along the plane), whereas the band at 561 cm^{-1} can be ascribed to the polarized A_{1g} mode (stretching vibration of oxygen atom perpendicular to the plane).[51] The peak intensity ratio resembles earlier reported γ-NiOOH phases containing lattice disorder and distorted interlayer spacing between the sheets.[52] In situ Ni displayed a similar feature that confirms the formation of an identical active structure during surface transformation. Furthermore, the peak at 600 cm^{-1} and broad features at around 780 and 900 cm^{-1} (magnified inset image) of the in situ Raman of Ni_2Si can be correlated with the $\nu(Si^{IV}—O^-)$, $\nu(Si—O—Si)$, and $\nu(Si—OH)$ vibrations.[53,54] These remaining silicon oxide species could potentially stabilize OER reaction intermediates and improve the kinetics, as it has been shown for surface adsorbed chalcogenide oxoanions previously.[55]

To determine the in situ oxidation states and to uncover structural features of the amorphous phase, in situ XAS analysis was performed. All in situ XAS were measured after OER-CP at 10 mA cm^{-2} for 24 h and freeze quenched at 1.58 V_{RHE} or 1.10 V_{RHE} (chronoamperometry). For both Ni and Ni_2Si, a clear shift of the Ni edge is observed, indicating the oxidation of the metallic precatalysts during OER is consistent with the other analytical investigations (Figure 4c). The half-edge of Ni_2Si appears at higher energy, revealing that a more oxidized γ-NiOOH phase is formed from the Ni_2Si precatalysts compared to Ni.[39] Further, the comparison of in situ XANES measurements at a potential below the Ni$^{II/III}$ redox feature (1.10 V_{RHE}) and those above this redox feature (1.58 V_{RHE}, see inset Figure 4c) shows a significantly larger difference for Ni_2Si than Ni indicating a higher Ni$^{II/III}$ redox activity for Ni_2Si.
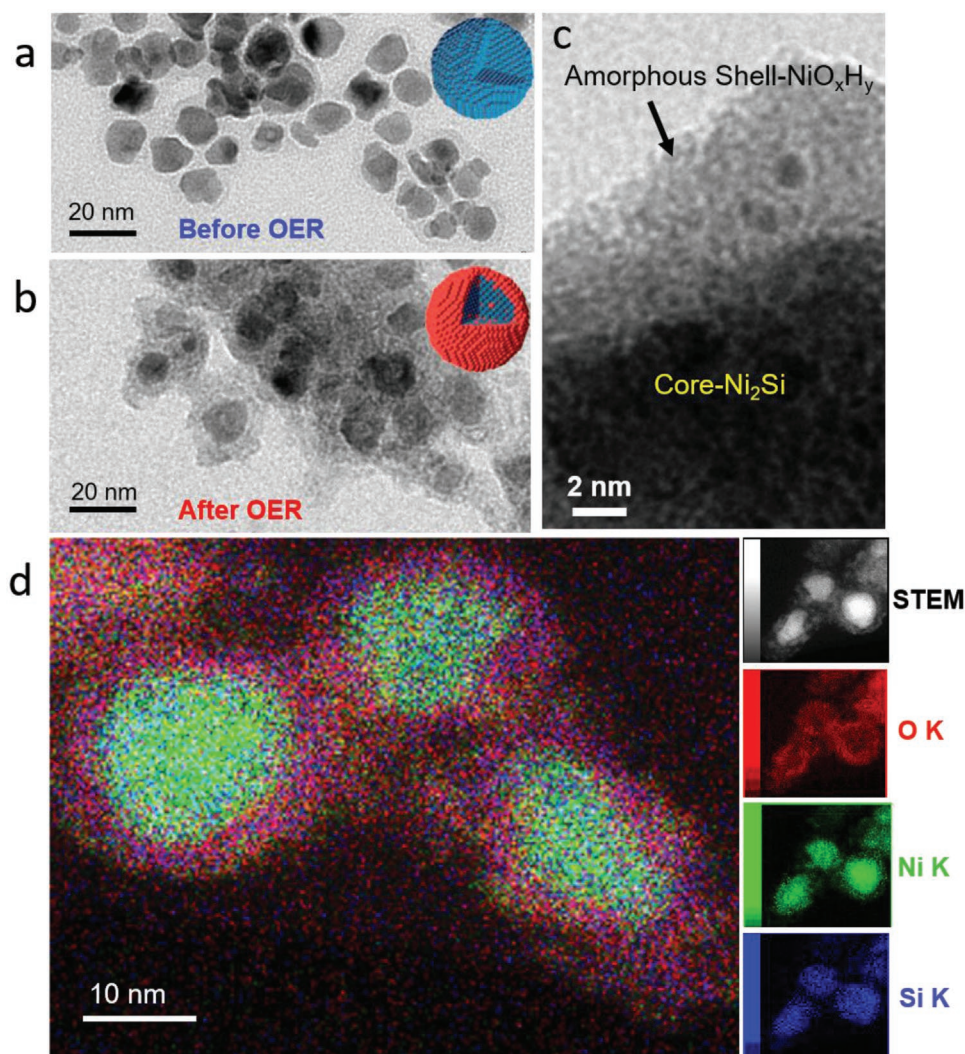
Figure 3. Post-OER structure of the Ni_2Si NPs. a,b) Before and after OER (CP for 24 at 10 mA cm^{-2} on Ni_2Si/FTO film) low-magnification TEM nanograph of Ni_2Si NP. After OER the Ni_2Si NPs were collected from the FTO substrate using ultrasonication in acetone. c) High-magnification TEM of a selected portion of after-OER Ni_2Si particle which covered under XRD-amorphous nickel(oxy)hydroxide shell in the form of a core-shell structure. d) TEM-EDX elemental mapping of after-OER Ni_2Si particles shows the distribution of Ni (green), Si (blue), and oxygen (red) around the core-shell structures.

For the as-prepared materials, the obtained EXAFS data was successfully simulated with a simplified model of the PXRD determined crystal structures of Ni_2Si and Ni (Figure 4d, Figures S58–S60 and Tables S7–S14, Supporting Information). For the samples after OER, the two closest shells of γ-NiOOH (Ni—O and Ni—Ni) were added. These shells represent the six O atoms coordinating a Ni center to form an [NiO$_6$] octahedron and the six closest Ni atoms. For Ni_2Si freeze quenched at 1.58 V$_{RHE}$, the population of these shells is around three instead of six, indicating that around half of the Ni atoms are in a coordination environment similar to γ-NiOOH. For Ni freeze quenched at 1.58 V$_{RHE}$, the population was around one, indicating that only around one-sixth of the Ni atoms are in a coordination environment similar to γ-NiOOH. Thus, the EXAFS result supports the hypothesis that in the case of Ni_2Si, more catalytically active γ-NiOOH was formed than in the case of Ni.

2.5. A General Model of the Active Catalyst Responsible for OER

From the ex situ and in situ analysis, we could show that under anodic potential, Ni_2Si acts as a precatalyst and undergoes partial corrosion deep inside the surface, which is in accordance with the Pourbaix diagram of Ni and Si. The dissolution of Si from the structure of Ni_2Si accompanied by the concomitant oxygen substitution resulted in the formation of an amorphous γ-NiOOH overlayer on the crystalline Ni_2Si core. The transformation of Ni_2Si into the γ-NiOOH phase occurs through the formation of Ni^{II} species.[56] We confirm this reconstruction of Ni_2Si using Raman spectra of different Ni_2Si/FTO films freeze-quenched at 30 s, 1 min, and 5 min under a constant potential of 1.5 V$_{RHE}$ (Figure S61, Supporting Information). The result displays the formation of nickel oxo species (mixture of α-Ni(OH)$_2$ and γ-NiOOH) within 1 min which thereafter transformed into the γ-NiOOH phase over prolong reaction time.
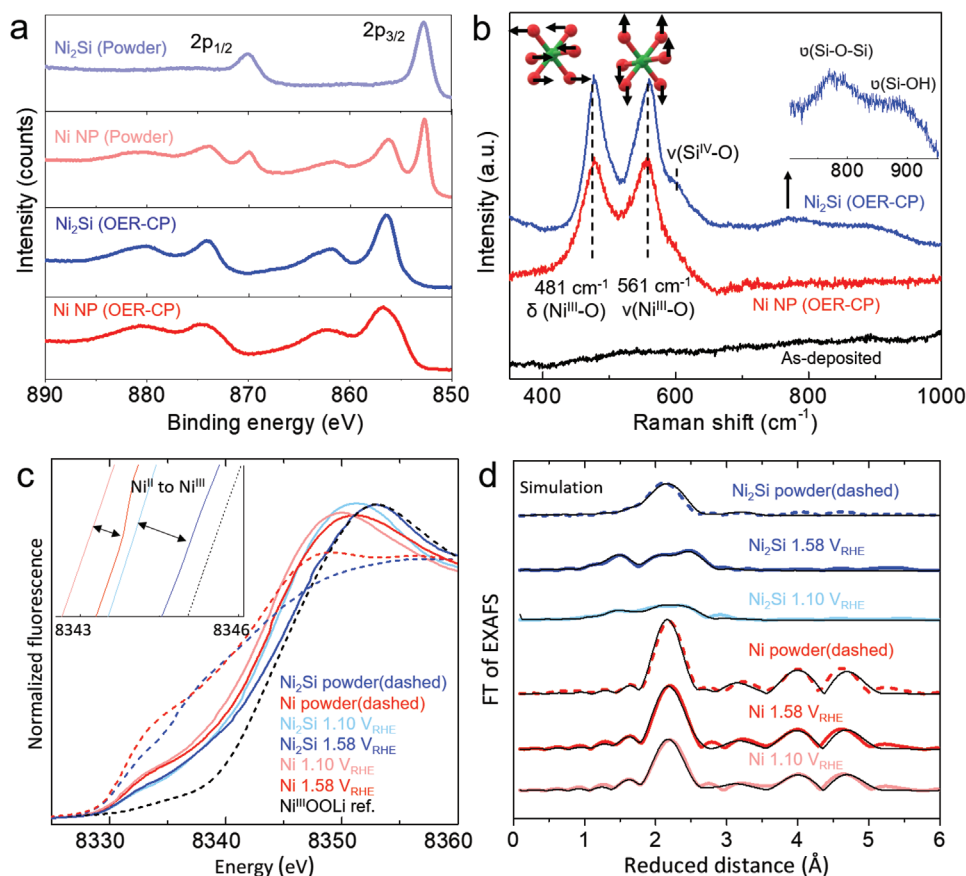
Figure 4. a) Before and after OER Ni 2p XPS profile of Ni NP and Ni$_2$Si NP. b) Quasi in situ and ex situ Raman spectroscopy of Ni$_2$Si and Ni NP (OER CA, 24 h) on FTO collected at a potential of 1.55 V$_{RHE}$ in alkaline electrolyte. Pristine Ni$_2$Si and Ni NPs are Raman inactive (Ni NPs are not shown here). The stretching A_{1g} (561 cm^{-1}) and bending E_g (481 cm^{-1}) vibrational modes of γ-NiOOH are represented by [NiO$_6$] octahedron (Ni is green and O is red). c) XANES measurements of the as-prepared powders and samples freeze quenched at two different potentials, the inset shows a magnification at around half of the edge maximum. d) EXAFS spectra of the same samples like in "panel c" with simulations in black.

Nevertheless, the active structure observed for both Ni$_2$Si and Ni NPs precatalysts was very similar, and in both cases, the formation of γ-NiOOH active catalyst is unavoidable. Based on the Bruke and O'Sullivan studies, the skeletal nature of this amorphous γ-NiOOH should be a major advantage from an electrocatalytic viewpoint as it permits a major increase in the number of oxycations participating in the electrode reaction.[57] The conceptual picture is that γ-NiOOH fragments with molecular dimensions are surrounded by electrolytes composed of water, anions, and cations. Continuous OER activity is maintained by conduction of the proton from the bulk catalyst phase to the bulk-electrolyte. The calculated turnover frequency values were 4.1×10^{-2} and 9.4×10^{-3} for Ni$_2$Si and Ni NP, respectively, at the η value of 300 mV (with FTO). Moreover, the similar Tafel slopes of both catalysts indicate the same kind of active sites. Hence, the activity difference is majorly caused by an unequal number of active sites. The higher activity of Ni$_2$Si than that of Ni NPs can be explained by the leaching of Si into the electrolyte that creates a large number of voids in the in situ formed NiOOH phase and enables more electrolyte permeability. Thus, not only the surface but also bulk Ni sites have access to the electrolyte and can participate in the catalytic process resulting in bulk catalytic activity.[58,59] Additionally, we tried to find a

metric that reflects the difference in the number of catalytically active sites. In this regard, we normalized the current density using the charge passed during the reverse scan of the Ni$^{II/III}$ redox peak for both Ni$_2$Si and metallic Ni. This normalization resulted in identical current density for Ni$_2$Si and metallic Ni (Figure S62, Supporting Information). Thus, in this case, the number of reversibly reducible Ni sites correlates well with the number of catalytically active sites, and both catalysts most likely have the same kind of active sites.

2.6. Oxidative Dehydrogenation of Organic Amines

Recently, replacing OER with organic transformation in an electrochemical cell has proven to be an effective approach for the simultaneous production of clean H$_2$ fuel at the cathode and value-added organic products at the anode, thus constructing a more efficient and economical water-splitting system.[60] The conventional OER kinetics is sluggish and requires high overpotentials to produce the low-value product oxygen. This facile hybrid water electrolysis approach can overcome the above problem, which basically requires lower oxidation potential than OER, and produces high-value

oxidation and reduction products at both the anode and the cathode, respectively.[23,61]

Herein, we coupled the OER with dehydrogenation of the organic amines, which offers an ideal platform to produce value-added nitriles together with augmenting green hydrogen production at the cathode. These nitrile functional groups can be found in various natural products, pharmaceuticals, and pesticides.[62] The typical synthesis of organocyanide compounds involves expensive noble metals and an organic compound with a leaving group by the substitution of stoichiometric toxic reagents such as KCN or CuCN.[63] Here we report the synthesis of cyanide compounds using non-precious materials under mild conditions. The electrooxidation of organic amines was carried out in 1 M KOH solution, and benzylamine (BA) was selected as the model substrate. **Figure 5**a shows the LSV curves of Ni_2Si in 1 M KOH with and without BA. After the addition of 50 mM BA into 1 M KOH solution, the LSV curve displayed a large redox sweep starting from 1.35 V_{RHE} (similar to Ni^{II}/Ni^{III}), followed by a steep rise in the OER region with an almost threefold increase of the current density value at 1.55 V.

Moreover, the onset potential displayed a shift of 48 mV after BA addition. This suggests that the electrocatalytic oxidation of BA is a more thermodynamically favorable reaction than OER and can be integrated with high-efficiency H_2 generation. We observed a rigorous H_2 gas bubble generation at the cathode starting from 1.37 V, attributing the reduction of additional H^+ originating from subsequent BA oxidation. On the other hand, for bare NF, the BA oxidation LSV showed a trivial increase of the current density value as compared to without BA. To explore the potential dependence of BA oxidation on Ni_2Si and to get a quantitative idea of the corresponding product, bulk electrolysis was carried out by applying a constant potential at 1.49 V_{RHE} in an undivided cell that started with a current density of 275 mA cm^{-2} in the presence of 50 mM BA in 10 mL 1 M KOH (Figure S63, Supporting Information). After 40 min of electrolysis at room temperature, it was observed that a 193 C charge was passed. The characterization of the reaction mixture of oxidation products by ^1H NMR spectroscopy reveals the complete conversion of BA to benzonitrile with an FE value of 99% (Figure 5c, Figure S64, Supporting Information). Notably, the
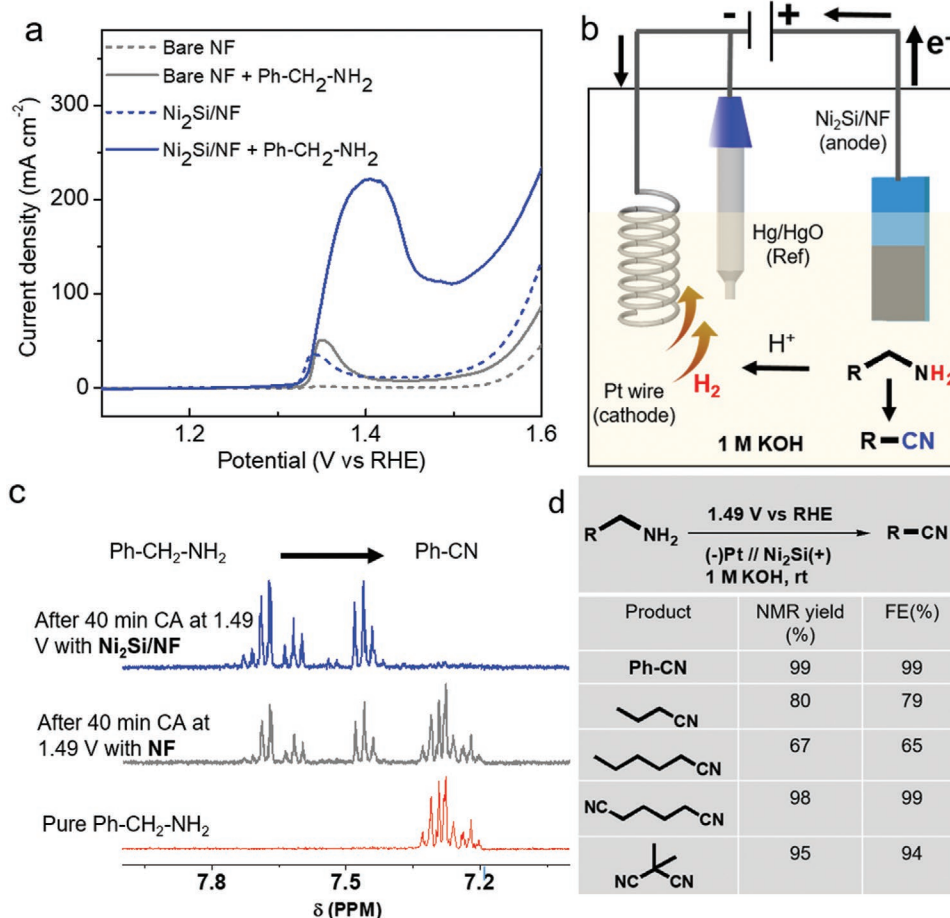
Figure 5. a) LSV of Ni_2Si/NF and bare NF in presence of 50 mM benzylamine solution (20 mL 1 M KOH) 1 mV s^{-1}. b) Bulk oxidation (dehydrogenation) of primary amines coupled with cathodic hydrogen evolution in an undivided cell. c) ^1H NMR tracking of the bulk oxidation of benzylamine at 1.49 V_{RHE} in 1 M KOH solution with Ni_2Si/NF and bare NF after 40 min (see Figure S63, Supporting Information, for the electrochemical chronoamperometry and Figure S64, Supporting Information, for full ^1H NMR spectra). d) Different substrate scope (50 mM) for the production of "nitriles" from their corresponding primary amines with Ni_2Si/NF anode in 1 M KOH (See Figure S66, Supporting Information, for LSV curves and Figures S67–S70, Supporting Information, for ^1H NMR recorded after bulk electrolysis at 1.49 V_{RHE}).

amount of H_2 gas evolution was ten-fold higher as compared to pristine OER condition (Figure S63, Supporting Information) and estimated as 67 wt.% H_2 based on amine content. Similarly, the control reaction was performed on bare NF under the same specified condition, which exhibited a 107.6 C charge passed after 40 min of electrolysis (Figure S63, Supporting Information). The corresponding ^1H NMR spectra of the reaction mixture confirmed a less than 50% conversion of BA (Figure 5c). The bulk electrolysis was further investigated at different potentials (at 1.41 V_{RHE} and 1.46 V_{RHE} which belong to the broad redox feature of the BA) and performed at the same time which indicates that the conversion rate increased with the increasing potential (Figure S63, Supporting Information). Additionally, the activity was compared with as-prepared NiS and Ni(OH)$_2$. The CV of the Ni(OH)$_2$/NF and NiS/NF in presence of 50 mm BA showed a typical redox peak for BA oxidation. The bulk electrolysis was carried out at 1.49 V_{RHE} and the product was determined using ^1H NMR spectroscopy after 40 min of the reaction, which showed 45% and 60% of the conversion of BA in benzonitrile for Ni(OH)$_2$ and NiS, respectively (Figure S65, Supporting Information). We then investigated the broader applicability of Ni$_2$Si anode for the oxidation of various aliphatic amines (Figure 5d). Butylamine and hexylamine were successfully oxidized to corresponding nitriles at a remarkably lower potential than that of OER on Ni$_2$Si (Figure S66, Supporting Information). With the help of ^1H NMR, the estimated FE for the conversion of butylamine and hexylamine was 79% and 65%, respectively (Figures S67 and S68, Supporting Information). Interestingly, the electrocatalytic oxidation of di-substituted aliphatic amines such as hexamethylenediamine and 2,2-dimethylpropane-1,3-diamine selectively yielded the corresponding aliphatic dicyanide products such as adiponitrile and 2,2-dimethylmalononitrile, respectively (Figures S69 and S70, Supporting Information). It should be noted that adiponitrile is a precursor to the nylon-6,6 polymer. The above results suggest that Ni$_2$Si is a low-cost and efficient electrocatalyst to oxidize aromatic or aliphatic amines to corresponding cyanide products with significantly lower overpotential compared to the OER, which may be integrated with high-efficiency H_2 generation for water electrolysis.

3. Conclusion

In conclusion, we have adopted a rational colloidal approach that has driven control diffusion of the Si atoms into Ni crystallites yielding well-defined Ni$_2$Si NPs. The as-prepared Ni$_2$Si has been employed as a promising OER electro(pre)catalyst displaying excellent activities and stabilities both on NF and FTO in 1 m Fe-free KOH electrolyte. Moreover, the phase transformation of Ni$_2$Si has been successfully monitored by the quasi in situ XAS and resonance Raman technique, which revealed a larger electrochemical transformation for Ni$_2$Si as compared to Ni NPs. The normalization of the LSV current density by BET surface area and C_{dl} produced by Ni$_2$Si and Ni clearly indicates that the catalytic activity was dominated by the amount of surface transformation. A similar Tafel slope, Raman bands, and EXAFS fit (with corresponding crystallographic parameters) confirms that Ni$_2$Si and Ni NPs feature an identical Ni^{III}O$_x$H$_y$ active phase, although the dissolution of Si (through e.g. oxide,

hydroxide, polysilicates) is expected to generate a more porous Ni^{III}O$_x$H$_y$ phase with a distorted layered structure and facilitate electrolyte penetration. Additionally, Ni$_2$Si in the activated form is highly efficient for electrooxidative dehydrogenation of primary amines into nitriles with the highest selectivity and broad substrate scope. The presented study would be helpful to develop a new class of solid-state intermetallic materials that were difficult to prepare in its nano-form and to understand the relationship between electrochemical transformation and catalytic activities of a wide variety of solid-state intermetallic materials for water splitting and electrochemical organic oxidation.

Supporting Information

Supporting Information is available from the Wiley Online Library or from the author.

Conflict of Interest

The authors declare no conflict of interest.

Data Availability Statement

The data that support the findings of this study are available from the corresponding author upon reasonable request.

[1] S. Klemenz, A. Stegmüller, S. Yoon, C. Felser, H. Tüysüz, A. Weidenkaff, *Angew. Chem., Int. Ed.* **2021**, *60*, 20094.

[2] H. Yang, M. Driess, P. W. Menezes, *Adv. Energy Mater.* **2021**, *11*, 2102074.

[3] S. Anantharaj, S. Noda, V. R. Jothi, S. C. Yi, M. Driess, P. W. Menezes, *Angew. Chem.* **2021**, *133*, 19129.

[4] Z. Y. Yu, Y. Duan, X.-Y. Feng, X. Yu, M.-R. Gao, *Adv. Mater.* **2021**, *33*, 2007100.

[5] M. Yu, E. Budiyanto, H. Tüysüz, *Angew. Chem., Int. Ed.* **2021**, *61*, e202103824.

[6] L. Yang, Z. Liu, S. Zhu, L. Feng, W. Xing, *Mater. Today Phys.* **2021**, *16*, 100292.

[7] C. Panda, P. W. Menezes, M. Driess, *Angew. Chem., Int. Ed.* **2018**, *57*, 11130.

[8] S. Song, L. Yu, X. Xiao, Z. Qin, W. Zhang, D. Wang, J. Bao, H. Zhou, Q. Zhang, S. Chen, Z. Ren, *Mater. Today Phys.* **2020**, *13*, 100216.

[9] K. Wan, J. Luo, X. Zhang, P. Subramanian, J. Fransaer, *J. Energy Chem.* **2021**, *62*, 198.

[10] Z.-J. Wang, M.-X. Jin, L. Zhang, A.-J. Wang, J.-J. Feng, *J. Energy Chem.* **2021**, *53*, 260.

[11] M. Zha, C. Pei, Q. Wang, G. Hu, L. Feng, *J. Energy Chem.* **2020**, *47*, 166.

[12] J. Bak, Y. Heo, T. G. Yun, S.-Y. Chung, *ACS Nano* **2020**, *14*, 14323.

[13] J. Zhou, L. Yu, Q. Zhou, C. Huang, Y. Zhang, B. Yu, Y. Yu, *Appl. Catal. B* **2021**, *288*, 120002.

[14] Y. Li, X. Bao, D. Chen, Z. Wang, N. Dewangan, M. Li, Z. Xu, J. Wang, S. Kawi, Q. Zhong, *ChemCatChem* **2019**, *11*, 5913.

[15] P. W. Menezes, C. Panda, S. Loos, F. Bunschei-Bruns, C. Walter, M. Schwarze, X. Deng, H. Dau, M. Driess, *Energy Environ. Sci.* **2018**, *11*, 1287.

[16] P. W. Menezes, S. Yao, R. Beltrán-Suito, J. N. Hausmann, P. V. Menezes, M. Driess, *Angew. Chem.* **2021**, *133*, 4690.

[17] R. D. L. Smith, C. P. Berlinguette, *J. Am. Chem. Soc.* **2016**, *138*, 1561.

[18] J. Masa, S. Piontek, P. Wilde, H. Antoni, T. Eckhard, Y.-T. Chen, M. Muhler, U.-P. Apfel, W. Schuhmann, *Adv. Energy Mater.* **2019**, *9*, 1900796.

[19] M. S. Burke, S. Zou, L. J. Enman, J. E. Kellon, C. A. Gabor, E. Pledger, S. W. Boettcher, *J. Phys. Chem. Lett.* **2015**, *6*, 3737.

[20] C. Walter, P. W. Menezes, M. Driess, *Chem. Sci.* **2021**, *12*, 8603.

[21] M. Armbrüster, R. Schlögl, Y. Grin, *Sci. Technol. Adv. Mater.* **2014**, *15*, 034803.

[22] P. W. Menezes, C. Walter, J. N. Hausmann, R. Beltrán-Suito, C. Schlesiger, S. Praetz, V. Y. Verchenko, A. V. Shevelkov, M. Driess, *Angew. Chem., Int. Ed.* **2019**, *58*, 16569.

[23] B. Chakraborty, R. Beltrán-Suito, J. N. Hausmann, S. Garai, M. Driess, P. W. Menezes, *Adv. Energy Mater.* **2020**, *10*, 2001377.

[24] P. W. Menezes, C. Panda, S. Garai, C. Walter, A. Guiet, M. Driess, *Angew. Chem., Int. Ed.* **2018**, *57*, 15237.

[25] R. Beltrán-Suito, V. Forstner, J. N. Hausmann, S. Mebs, J. Schmidt, I. Zaharieva, K. Laun, I. Zebger, H. Dau, P. W. Menezes, M. Driess, *Chem. Sci.* **2020**, *11*, 11834.

[26] E. G. Colgan, M. Mäenpää, M. Finetti, M.-A. Nicolet, *J. Electron. Mater.* **1983**, *12*, 413.

[27] S. Z. Han, J. Kang, S. D. Kim, S.-Y. Choi, H. G. Kim, J. Lee, K. Kim, S. H. Lim, B. Han, *Sci. Rep.* **2015**, *5*, 15050.

[28] P. J. Grunthaner, F. J. Grunthaner, *J. Vac. Sci. Technol.* **1982**, *20*, 680.

[29] R. Kumar, M. Bahri, Y. Song, F. Gonell, C. Thomas, O. Ersen, C. Sanchez, C. Laberty-Robert, D. Portehault, *Nanoscale* **2020**, *12*, 15209.

[30] Y. Song, S. Casale, A. Miche, D. Montero, C. Laberty-Robert, D. Portehault, *J. Mater. Chem. A* **2022**, *10*, 1350.

[31] Y. Li, X. Wei, L. Chen, *Angew. Chem., Int. Ed.* **2021**, *60*, 19550.

[32] R. D. Patil, M. K. Gupta, *Adv. Synth. Catal.* **2020**, *362*, 3987.

[33] M. Largeron, *Eur. J. Org. Chem.* **2013**, *2013*, 5225.

[34] G. Y. Popova, T. V. Andrushkevich, Y. A. Chesalov, L. M. Plyasova, L. S. Dovlitova, E. V. Ischenko, G. I. Aleshina, M. I. Khramov, *Catal. Today* **2009**, *144*, 312.

[35] Y. Huang, X. Chong, C. Liu, Y. Liang, B. Zhang, *Angew. Chem., Int. Ed.* **2018**, *57*, 13163.

[36] F. Léonard, A. A. Talin, *Nat. Nanotechnol.* **2011**, *6*, 773.

[37] L. Trotochaud, S. L. Young, J. K. Ranney, S. W. Boettcher, *J. Am. Chem. Soc.* **2014**, *136*, 6744.

[38] J. N. Hausmann, R. Beltrán-Suito, S. Mebs, V. Hlukhyy, T. F. Fässler, H. Dau, M. Driess, P. W. Menezes, *Adv. Mater.* **2021**, *33*, 2008823.

[39] J. Massa, I. Sinev, H. Mistry, E. Ventosa, M. de la Mata, J. Arbiol, M. Muhler, B. R. Cuenya, W. Schuhmann, *Adv. Energy Mater.* **2017**, *7*, 1700381.

[40] A. G. Rajan, E. A. Carter, *Energy Environ. Sci.* **2020**, *13*, 4962.

[41] S. Anantharaj, S. Noda, M. Driess, P. W. Menezes, *ACS Energy Lett.* **2021**, *6*, 1607.

[42] C. C. L. McCrory, S. H. Jung, J. C. Peters, T. F. Jaramillo, *J. Am. Chem. Soc.* **2013**, *135*, 16977.

[43] D. K. Bediako, B. L. Kaiser, Y. Surendranath, J. Yano, V. K. Yachandra, D. G. Nocera, *J. Am. Chem. Soc.* **2012**, *134*, 6801.

[44] Z. Yan, H. Sun, X. Chen, H. Liu, Y. Zhao, H. Li, W. Xie, F. Cheng, J. Chen, *Nat. Commun.* **2018**, *9*, 2373.

[45] P. W. Menezes, A. Indra, C. Das, C. Walter, C. Gobel, V. Gutkin, D. Schmeisser, M. Driess, *ACS Catal.* **2017**, *7*, 103.

[46] C. W. Hu, Y. Yamada, K. Yoshimura, *J. Mater. Chem. C* **2016**, *4*, 5390.

[47] X. Z. Fu, Y. J. Zhu, Q. C. Xu, J. Li, J. H. Pan, J. Q. Xu, J. D. Lin, D. W. Liao, *Solid State Ionics* **2007**, *178*, 987.

[48] R. V. Pushkarev, N. I. Fainer, V. V. Kaichev, T. Goto, *Mater. Des.* **2018**, *137*, 422.

[49] D. S. Hall, D. J. Lockwood, C. Bock, B. R. MacDougall, *Proc. R. Soc. London, Ser. A* **2015**, *471*, 20140792.

[50] B. M. Hunter, W. Hieringer, J. R. Winkler, H. B. Gray, A. M. Muller, *Energy Environ. Sci.* **2016**, *9*, 1734.

[51] Y. L. Lo, B. J. Hwang, *Langmuir* **1998**, *14*, 944.

[52] S. Lee, L. Bai, X. Hu, *Angew. Chem., Int. Ed.* **2020**, *59*, 8072.

[53] S. W. da Silva, R. C. Pedroza, P. P. C. Sartoratto, D. R. Rezende, A. V. da Silva Neto, M. A. G. Soler, P. C. Morais, *J. Non-Cryst. Solids* **2006**, *352*, 1602.

[54] C. A. Murray, T. J. Greytak, *Phys. Rev. B* **1979**, *20*, 3368.

[55] J. N. Hausmann, P. W. Menezes, *Curr. Opin. Electrochem.* **2022**, *34*, 100991.

[56] J. Huang, Y. Li, Y. Zhang, G. Rao, C. Wu, X. Wang, R. Lu, Y. Li, J. Xiong, *Angew. Chem., Int. Ed.* **2019**, *58*, 17458.

[57] L. D. Burke, E. J. M. O'Sullivan, *J. Electroanal. Chem.* **1981**, *117*, 155.

[58] J. N. Hausmann, S. Mebs, K. Laun, I. Zebger, H. Dau, P. W. Menezes, M. Driess, *Energy Environ. Sci.* **2020**, *13*, 3607.

[59] K. Klingan, F. Ringleb, I. Zaharieva, J. Heidkamp, P. Chernev, D. Gonzalez-Flores, M. Risch, A. Fischer, H. Dau, *ChemSusChem* **2014**, *7*, 1301.

[60] L. Du, Y. Sun, B. You, *Mater. Rep.: Energy* **2021**, *1*, 100004.

[61] B. Mondal, N. Karjule, C. Singh, R. Shimoni, M. Volokh, I. Hod, M. Shalom, *Adv. Mater.* **2021**, *11*, 2101858.

[62] F. F. Fleming, L. Yao, P. C. Ravikumar, L. Funk, B. C. Shook, *J. Med. Chem.* **2010**, *53*, 7902.

[63] P. Anbarasan, T. Schareina, M. Beller, *Chem. Soc. Rev.* **2011**, *40*, 5049.